Applied Catalysis B: Environmental 260 (2020) 118189

Contents lists available at ScienceDirect

Applied Catalysis B: Environmental

journal homepage: www.elsevier.com/locate/apcatb

Integrating photocatalysis and thermocatalysis to enable efficient CO_2 reforming of methane on Pt supported CeO_2 with Zn doping and atomic layer deposited MgO overcoating

Fuping Pan[a], Xianmei Xiang[a], Zichen Du[a], Erik Sarnello[b], Tao Li[b,c], Ying Li[a,*]

[a] J. Mike Walker '66 Department of Mechanical Engineering, Texas A&M University, College Station, TX, 77843, United States
[b] Department of Chemistry and Biochemistry, Northern Illinois University, DeKalb, IL, 60115, United States
[c] Chemistry and Material Science Group, X-ray Science Division, Argonne National Laboratory, Lemont, IL, 60439, United States

ARTICLE INFO

Keywords:
Dry reforming
Photocatalysis
Stability
Doping
Atomic layer deposition

ABSTRACT

CO_2 reforming or dry reforming of methane (DRM) produces syngas with a low carbon footprint, but the efficiency and stability of DRM remains a challenge. Herein, we report an efficient photo-thermo-chemical DRM (PTC-DRM) process on a Pt supported CeO_2 catalyst with Zn doping and surface atomic layer deposition (ALD)-enabled MgO overcoating using concentrated sunlight as the energy input. Under 30 suns irradiation at 600 °C, high syngas production rates of 356 and 516 mmol g^{-1} h^{-1} for H_2 and CO are achieved, which are more than 9 and 3 times larger than those obtained in the thermally driven DRM. Moreover, the light illumination stabilizes the dry reforming process without deactivation, which results from the in situ generation of oxygen vacancy on CeO_2 by photo-induced electrons that enables stable CO_2 thermo-activation. The ALD coating also reduces surface charge recombination through passivating surface states, thereby enhancing photocatalytic activity.

1. Introduction

CO_2 reforming of methane, also called drying reforming of methane (DRM), is an alternative way of producing syngas (H_2 and CO) to conventional steam reforming of methane. [1,2] Syngas is a valuable product that can be further converted into liquid fuels through Fischer-Tropsch processes [3]. However, DRM is an extremely endothermic reaction and requires tremendous energy input to attain high equilibrium conversions [1]. Thermocatalytic DRM using thermal energy from fossil fuels has been widely studied, but it is extremely energy-consuming and leads to the re-emission of greenhouse gases. Even when renewable energy such as solar is applied in DRM, solar energy is used as a heat source, neglecting the high energy potential of photons in the UV or near UV regions. [4] Recently, a few photocatalytic DRM reports are available in the literature, which utilizes photocatalytically induced charges to accomplish the reaction [5–8]. Unfortunately, most research in this direction was conducted at low temperatures using a low solar irradiation intensity. As a result, the yield of syngas production is typically very low, far from industrial application requirements [6,9].

Very recently, a new approach of photo-thermo-chemical DRM (PTC-DRM) has been proposed to improve DRM efficiency by coupling solar energy and thermal energy in one reactor. [10–12] The PTC-DRM conducted at high temperatures has demonstrated a significant boost in DRM activity under photo-illumination compared with that under dark at the same temperature. However, the catalytic synergy between photocatalysis and thermocatalysis is still not well understood, and the application of using concentrated solar to power PTC-DRM reaction is limited [10,11]. By using concentrated solar, the thermal energy needed to activate thermocatalytic reactions and the low-wavelength photons needed to activate photocatalytic reactions are simultaneously available, and thus making PTC-DRM a potentially competitive technology for converting greenhouse gases into fuels at a large scale. The development of an appropriate catalyst that can efficiently utilize both thermal and photon energy is the key to the emerging PTC-DRM reaction. Previous reports demonstrated that Pt supported CeO_2, TiO_2, or TaN were appropriate catalysts, where Pt was the thermocatalytic DRM catalyst and co-catalyst for photocatalysis while CeO_2, TiO_2, or TaN were the DRM supports and semiconductor photocatalysts. [10–12] Despite these advancements, developing high-performance photo-thermally active catalysts is still highly needed to achieve improved syngas production.

In general, a key factor limiting PTC-DRM performance is the fast recombination of photo-generated electrons and holes, leading to low numbers of available charge carriers and thus their utilization

* Corresponding author.
E-mail address: yingli@tamu.edu (Y. Li).

https://doi.org/10.1016/j.apcatb.2019.118189
Received 25 May 2019; Received in revised form 20 August 2019; Accepted 12 September 2019
Available online 13 September 2019
0926-3373/

efficiency. [10,11] It has been widely proposed that appropriate doping can suppress the charge carriers recombination by creating some localized band states. For example, introducing nitrogen, zinc, and iron as secondary heteroatoms into TiO_2 or CeO_2 lattices can drastically boost their photocatalytic activity in CO_2 photoreduction and organic photodegradation. [13–17] Moreover, surface electronic states, formed owing to the changed periodicity of the crystalline solid and the missing binding partners, is also thought to be a trapping center for electrons [18,19]. To reduce the surface state density, a passivating overlayer has been applied [20]. Benefiting from the unique merits to enable atomic layers with controllable thickness, atomic layer deposition (ALD) technology is believed a powerful approach to deposit coating on catalysts surface. For instance, ALD-deposited Al_2O_3 and MgO coatings have been employed to passivate surface states of TiO_2 for ambient photocatalytic CO_2 reduction; [21,22] and an ALD-grown TiO_2 overlayer has also been loaded on Ta_3N_5 photoanode to remove surface state for photoelectrochemical water oxidation. [18] Besides benefits to photocatalysis, ALD-enabled surface coating was also effective in improving thermocatalytic DRM performance. Previous studies showed that ALD-deposited MgO layer was capable of improving thermal DRM activity and stability of nickel nanoparticles because MgO has high affinity to CO_2 and high basicity to decrease carbon deposition via promoting the reverse CO disproportionation [23].

Inspired by the above understanding, we hypothesized that the integration of both Zn doping and surface MgO coating would be effective for propelling PTC-DRM activity of photothermally active catalysts since these modifications could enhance catalytic capability for both photocatalysis and thermocatalysis. In this work, as a proof of concept, we selected Pt supported CeO_2 as a model catalyst to explore the effects of Zn doping and surface MgO modification on PTC-DRM performance. The in-situ Zn doping was achieved by introducing Zn during the synthesis of CeO_2 support, and the surface MgO overcoating was applied by the ALD method. These modulations in catalyst morphology, surface chemical states, optical properties, as well as PTC-DRM activity was systematically investigated. Moreover, we explored the influences of light irradiation on DRM stability, and the contribution from light illumination in promoting PTC-DRM stability was elucidated by comparing the structure and compositions changes of spent catalysts with and without light irradiation. Finally, the possible synergistic photo-thermo-catalysis DRM mechanism was proposed.

2. Experimental section

2.1. Catalysts synthesis

2.1.1. Synthesis of Zn-CeO_2 support

The best-performing Zn-doped CeO_2 (Zn-CeO_2) support with a Zn/Ce molar ratio of 0.1 was prepared by a modified citrate sol-gel method. Typically, a surfactant solution was prepared by dissolving 1.82 g of cetyltrimethylammonium bromide (CTAB) in 15 ml ethanol with ultrasound treatment. A precursor solution was prepared by dissolving 2.17 g $Ce(NO_3)_3$•$6H_2O$, 0.1487 g $Zn(NO_3)_3$·$6H_2O$, and 0.96 g citric acid in 5 ml ethanol. The precursor solution was then added into the surfactant solution drop-by-drop with vigorous stirring at room temperature. After stirring for another 4 h, the mixed solution was transferred to a Petri dish covered with PE film, which was placed in an oven at 60 °C to age for 48 h. The dried gel was then calcined at 500 °C for 5 h at a heating rate of 1 °C min^{-1} to crystallize CeO_2 and remove organic precursor, [24] forming the final Zn-CeO_2. To optimize PTC-DRM activity, Zn/Ce molar ratio was tuned from 0.05 to 0.2 by adjusting Zn $(NO_3)_3$·$6H_2O$ amounts in the precursor solutions while fixing Ce $(NO_3)_3$•$6H_2O$ amount. For comparison, Zn-free CeO_2 was also prepared using the same method as to Zn-CeO_2 except without adding Zn $(NO_3)_3$·$6H_2O$.

2.1.2. Synthesis of Pt/Zn-CeO_2

1 wt% Pt supported on Zn-CeO_2 (Pt/Zn-CeO_2) was synthesized by a wet impregnation method. Specifically, 100 mg as-prepared Zn-CeO_2 was dispersed in 5 ml ethanol under sonication for 10 min. Then, 4.2 ml H_2PtCl_6 aqueous solution (0.5 mg_{Pt} ml^{-1}) was added into the above solution. The mixture was continuously stirred at room temperature until the formation of dried powder, followed by calcination at 500 °C for 2 h with a heating rate of 1 °C min^{-1} to produce the final Pt/Zn-CeO_2 catalyst. CeO_2 and other Zn-CeO_2 supports were also used to load Pt.

2.1.3. Synthesis of MgO/Pt/Zn-CeO_2

To obtain 5 layers MgO coated Pt/Zn-CeO_2 (MgO/Pt/Zn-CeO_2), a commercial ALD system (Savannah S200, Ultratech) was applied. For each coating process, Pt/Zn-CeO_2 powders were loaded into a home-designed particle holder, which was placed in the middle of the reaction chamber of the ALD. To ensure adequate coating on porous materials, the ALD system was set in an “expo mode” assisted with a soft pump, which can prolong the time for precursor molecules to contact with the surface of ANR by slowing down the pressure decreasing rate. The pulse time of both H_2O and bis(ethylcyclopentadienyl)magnesium was 2 s with 5 cycles, and the reaction chamber was set at 200 °C. After ALD coating, the powder catalyst was further calcined at 500 °C for 1 h to remove any potential organic residues from the ALD process. [22] We also adjusted ALD cycles from 2 to 15 cycles to optimize PTC-DRM activity.

2.2. Catalysts characterization

The morphology, crystal structure, and chemical composition of the prepared catalysts were characterized by scanning electron microscopy (SEM, JEOL JSM7500 F), transmission electron microscopy (TEM, FEI Tecnai G2 F20 ST), X-ray diffraction (XRD, BRIKER D8), and X-ray photoelectron spectroscopy (XPS, Omicron). UV–vis diffuse reflectance spectra were collected by a Hitachi U4100 UV–vis-NIR Spectrophotometer with Praying Mantis accessory. Photoluminescence (PL) spectra were recorded on a PTI QuantaMaster series Spectrofluorometer using 300 nm incident light, and a 380 nm long pass filter was applied to the detector. Because PTC-DRM activity was evaluated after reducing catalysts in H_2/Ar mixture at 600 °C for 2 h, all catalysts were characterized after H_2/Ar post-treatment.

2.3. PTC-DRM experiments

PTC-DRM reaction was carried out in a tube reactor system as illustrated in Fig. S1, which mainly includes a concentrated solar simulator (ScienceTech Inc.) and a split tube furnace-powered quartz tube reactor (Applied Test Systems). A Sciencetech 200-1 K lamp housing with custom modular optics enclosures was used to provide controllable continuous concentrated broad spectrum. The irradiance can be adjusted by tuning working power (Fig. S2); operating at 300, 600, 900, and 1200 W are equivalent to 8, 15, 23, and 30 suns, respectively. There is a window on the furnace, which allows the incident light to irradiate catalyst surface. The quartz tube reactor with an inner diameter of 22 mm is placed in the chamber of the tube furnace. The catalyst holder is a piece of quartz frit (QPD30-0, Technical Glass Products) hosted in a quartz tube with an oval shape (24 mm × 16 mm) and a 45° bevel angle, giving an effective area of 3 cm^2 exposed to the incident light. A thermocouple in contact with the catalyst surface was directly connected to the furnace to monitor temperature and provide feedback to the power supply, ensuring the same reaction temperature in the dark and under light. For example, the light only can reach about 420 °C under light irradiation at 1200 W. To reach 600 °C under light, the furnace temperature was set to 600 °C, and thus the furnace would provide additional heat to reach the designated reaction temperatures. In the dark or the light was off, the thermal energy was only supplied

from the furnace itself.

In each experiment, 5 mg catalyst powder was first dispersed in 4 ml water and sonicated to form a uniform ink, which was then dropped on a piece of Whatman™ Quartz grade Filter paper and suspended on the oval catalyst holder, followed by drying at 60 °C overnight. The catalyst holder loaded with dried catalyst was then transferred into a quartz tube reactor. In each DRM experiment, the catalyst was first reduced in a mixed flow of H_2 (23 sccm) and Ar (28 sccm) for 2 h at 600 °C. The reactor was then purged by Ar for 1 h at 100 sccm to remove residual H_2, followed by introducing reaction gas (10%CO_2/10%CH_4/80%Ar) at a flow rate of 14 sccm. The gas mixture after reaction in the dark or under light was analyzed by an on-line Gas Chromatograph (GC 2010, Shimadzu) equipped with an automated gas valve and a thermal conductivity detector (TCD, to measure CO_2, CO, and H_2) and a flame ionization detector (FID, to measure CH_4). Only CO and H_2 were detected as the products; no other products such as hydrocarbons were detected.

The gas production rate normalized by the catalyst mass (n, mol $g^{-1} h^{-1}$) was calculated based on the following formula:

$$n = (P \cdot V \cdot v_i)/(R \cdot T)/m \times 3600$$

Where P is the pressure (1.01×10^5 Pa), V is the gas volumetric flow rate (2.3×10^{-7} m^3 s^{-1}), v_i is the volume concentration of gas product determined by GC, T is the temperature (298.15 K), R is the gas constant (8.314 J mol^{-1} K^{-1}), and m is the catalyst mass used (5×10^{-3} g).

3. Results and discussion

3.1. Structure, composition, and optical properties of catalysts

The structure of catalysts was first investigated by X-ray diffraction (XRD), which identifies the typical face-centered cubic fluorite structure of CeO_2 for Pt/CeO_2, Pt/Zn-CeO_2, and MgO/Pt/Zn-CeO_2 (Fig. 1a). Note that no diffraction peaks for Pt, Zn, and MgO were detected by XRD, probably owing to their low volume fractions. Morphology of MgO/Pt/Zn-CeO_2 was characterized by scanning electron microscopy (SEM) and transmission electron microscopy (TEM). An SEM image shows the spherical, irregular shape of powder samples, and the elemental mapping images identify the existence of Ce, Mg, Zn, and Pt (Fig. S3). A TEM image of MgO/Pt/Zn-CeO_2 exhibits the aggregated particles with an average particle size of 10 nm (Fig. 1b), and a high-resolution TEM image further demonstrates a typical interplanar lattice spacing of 0.31 nm (Fig. 1c), corresponding to the (111) plane of CeO_2 at 28.6° in the XRD pattern. Moreover, no noticeable MgO overcoating was observed, because 5 cycles of ALD is only able to deposit sub-nanometer MgO overcoating. [22] To further confirm this, we did TEM characterization for Pt/Zn-CeO_2 which did not have ALD-coated MgO. As shown in Fig. S4, Pt/Zn-CeO_2 exhibited the same feature as compared to MgO/Pt/Zn-CeO_2 (Fig. 1b,c), directly indicating that MgO coating does not change the surface morphology of Pt/Zn-CeO_2. Due to the atomic thin nature, it has been widely demonstrated that ALD-deposited overcoating will not block the light penetration and can be used to facilitate charge carriers separation by passivating surface states density. [18,21,22]

X-ray photoelectron spectroscopy (XPS) was further carried out to detect the surface composition. As shown in Fig. 1d, Pt/Zn-CeO_2 and MgO/Pt/Zn-CeO_2 showed obvious peaks at 1020.8 eV of Zn $2p_{3/2}$, whereas Pt/CeO_2 did not show Zn peak. This suggests the successful incorporation of Zn into CeO_2. Accordingly, only MgO/Pt/Zn-CeO_2 displayed Mg 2p peak at 49.8 eV corresponding to Mg^{2+} oxidation state (Fig. 1e), indicating the coating of MgO on the surface of Pt/Zn-CeO_2 by ALD. In addition, the existence of Pt on all three catalysts can be manifested from Pt 4f XPS spectra (Fig. S5), where the peak at 73.7 eV represents metallic Pt. Based on composition and preparation strategy, we proposed a schematic in Fig. 1f showing the structure of MgO/Pt/Zn-CeO_2. The photoactive support was composed of Zn-doped CeO_2

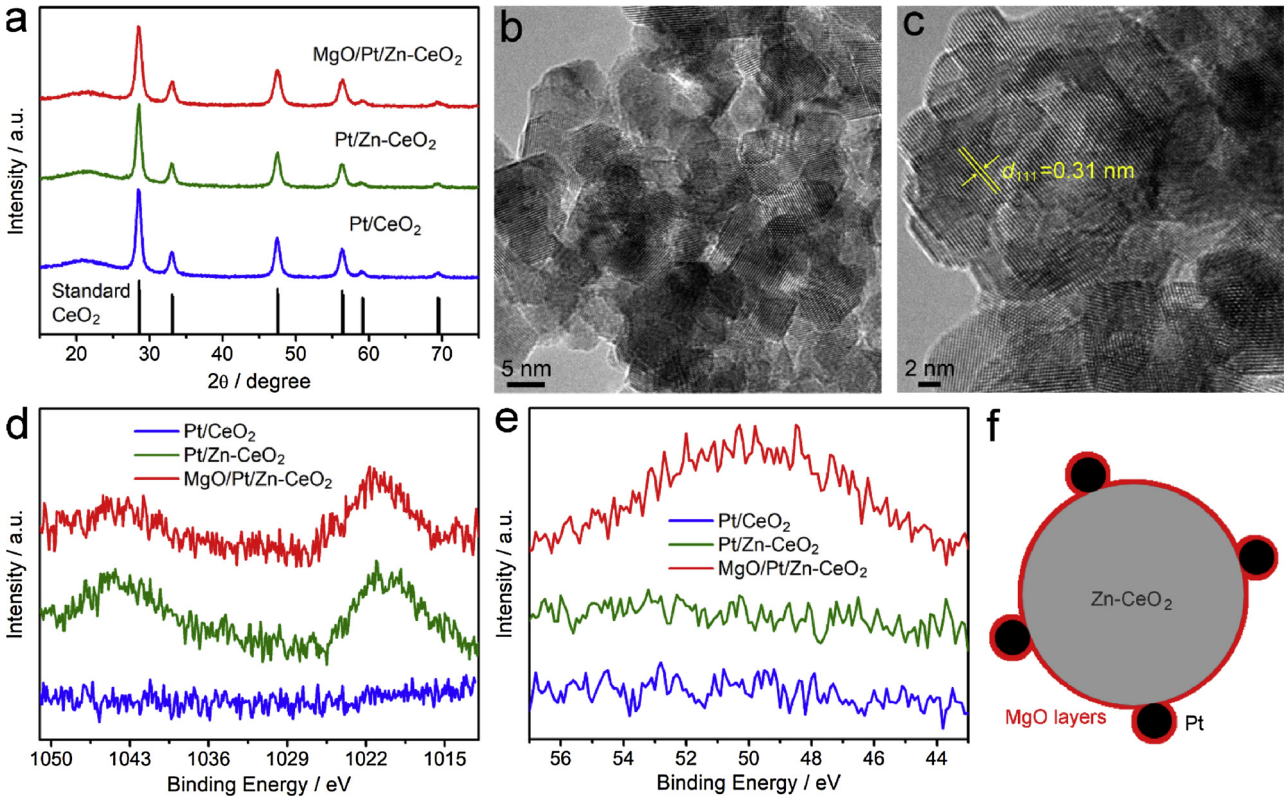

Fig. 1. XRD patterns of Pt/CeO_2, Pt/Zn-CeO_2, and MgO/Pt/Zn-CeO_2. (b) TEM and (c) HRTEM images of MgO/Pt/Zn-CeO_2. (d) Zn 2p and (e) Mg 2p XPS spectra of Pt/CeO_2, Pt/Zn-CeO_2, and MgO/Pt/Zn-CeO_2. (f) Proposed structural schematic of MgO/Pt/Zn-CeO_2.

prepared using a modified citrate sol-gel method; Pt, uniformly loaded on Zn-CeO_2 through wet impregnation, served as thermocatalytic component and co-catalyst for photocatalysis, and atomic MgO layers were covered on the surface of Pt/Zn-CeO_2 by ALD. This unique structure thus realizes the integration of Zn doping and surface MgO overcoating for Pt/CeO_2 modification, which are expected as synergistic promoters to boost PTC-DRM.

The optical properties were determined by recording UV–vis absorption spectra (Fig. S6a,6c), which show that the light absorption of Pt/Zn-CeO_2 is highly dependent on Zn contents in precursors and numbers of ALD cycles used to deposit MgO layers. We found that the small amount of Zn doping with a Zn:Ce molar ratio of 0.05 delivers the highest light absorption. This can be attributed to the generation of defects (such as oxygen vacancy) that has been demonstrated to be beneficial for increasing light adsorption capability of metal oxide photocatalysts. [25] However, more Zn doping had a negative influence on light absorption. As for effects of MgO coating, it was observed that the 2 cycle MgO coating declines the UV–vis absorption, while it can be enhanced with increased ALD cycles above 5.

The band gaps were further calculated based on Kubelka − Munk plots (Fig. 2a, Fig. S7b,S7d), which shows that Zn doping narrows the band gap of Pt/CeO_2, whereas MgO coating increases the band gap of Pt/Zn-CeO_2. Specifically, Pt/CeO_2 showed a band gap of 2.89 eV, which decreases to 2.83 eV with a Zn:Ce molar ratio of 0.1 and to 2. 73 eV with a Zn:Ce molar ratio of 0.2. On the other hand, the band gap of Pt/Zn-CeO_2 increases from 2.83 to 2.87 eV after 5 cycles MgO coating and to 2.92 eV after 15 cycles MgO overcoating. The reason for the decrease in band gap upon Zn doping might be because incorporating Zn into CeO_2 lattice could make oxygen atoms to be removed more easily as a result of enhanced lattice relaxation and decrease in the coordination around the Ce cations in the lattice of CeO_2 [26,27]. Conversely, the MgO coating on the surface of Pt/Zn-CeO_2 slightly inhibits the elimination of oxygen atoms due to surface protection, leading to less oxygen vacancy generated and therefore larger band gaps. [21] Unexpectedly, we found that Pt/0.2Zn-CeO_2 showed the lowest light adsorption but the smallest band gap. This may be because that, when more Zn was incorporated in CeO_2, the ZnO/CeO_2 composite may be formed, which may significantly alter the intrinsic light adsorption ability and electronic structure of CeO_2. The similar phenomenon has been observed on $BiVO_4$/CeO_2 composite reported by Chen and coworkers, [28] in which the $BiVO_4$/CeO_2 composite showed lower light adsorption and a smaller band gap as compared to $BiVO_4$.

Photoluminescence (PL) was further carried out to examine the influence of Zn doping and MgO overcoating on charge recombination properties. Since PL emission spectrum is derived from the recombination of excited charges, a lower PL intensity suggests a promoted charge separation. [29,30] As shown in PL spectra (Fig. 2b), Pt/Zn-CeO_2 displayed a lower intensity of emission peak than Pt/CeO_2, which was further lowered on MgO/Pt/Zn-CeO_2. It was also found that a higher Zn concentration and a larger ALD MgO cycle gave rise to lower PL intensities (Fig. S7). This implies that a promoted separation of photogenerated electrons and holes was achieved upon Zn doping and MgO coating. The role of Zn can be attributed to the creation of more defects, which serve as electron trap to suppress the recombination of electrons and holes. [30] Regarding the role of MgO layers, it is widely accepted that atomic metal oxides can promote charge carriers separation by passivating surface state [18], which might also work in our case. The enhanced charge carriers separation can improve the utilization efficiency of photogenerated charge carriers, providing more available charge carriers that can participate in the activation of CO_2 and CH_4 in the PTC-DRM process. [25]

3.2. Photo-thermo-catalytic DRM activity

The PTC-DRM activity was then evaluated using a custom-made reactor with a flow-bed mode powered by concentrated solar and furnace. The solar simulator, operated at 1200 W, can provide light irradiation equivalent to approximately 30 suns, which results in a temperature of 420 °C on the catalyst surface. Auxiliary heat from the furnace was thus supplied to reach designated reaction temperatures. For comparison purposes, DRM was also conducted in the dark to demonstrate the positive effects of photocatalytic contribution. Fig. 3**a,3b** display the H_2 and CO production rates in the dark and under light at 600 °C. Pt/CeO_2 exhibited initial H_2 and CO yields of 31 and 119 mmol $g^{-1}h^{-1}$ in the dark, respectively. The thermal DRM yields further reached 35 mmol $g^{-1}h^{-1}$ for H_2 and 127 mmol $g^{-1}h^{-1}$ for CO on Pt/Zn-CeO_2, as well as 37 mmol $g^{-1}h^{-1}$ for H_2 and 134 mmol $g^{-1}h^{-1}$ for CO on MgO/Pt/Zn-CeO_2. These results suggest that Zn doping and surface MgO decoration slightly expedites the thermocatalytic DRM process, which can be partially attributed to the enhanced interaction between Pt and CeO_2 after incorporating Zn doping and atomic MgO surface coating on Pt/CeO_2. The previous report has demonstrated that the strong metal-support interaction (such as Ni-CeO_2) could be able to promote the reactivity of metals towards thermocatalytic methane dissociation. [31]

When the DRM was carried out under light irradiation at the same temperature of 600 °C, the H_2 and CO production rates were significantly increased compared with those obtained in the thermal-driven DRM. The enhancement factors, calculated by dividing products yields obtained in the dark by products yields recorded under light, on Pt/CeO_2 and Pt/Zn-CeO_2 are 1.9 and 4.7 for H_2 as well as 1.5 and 2.6 for CO, respectively. More typically, MgO/Pt/Zn-CeO_2 showed H_2 and CO production rates reaching 356 and 516 mmol $g^{-1}h^{-1}$, which are 9.5 and 3.9 times higher compared to those obtained in the dark. It is obvious that both Zn doping and surface MgO modification play crucial roles in boosting the PTC-DRM activity of Pt/CeO_2. This can be ascribed to the integrated modification that creates defects and passivates surface states, thus facilitating the separation of photogenerated electrons

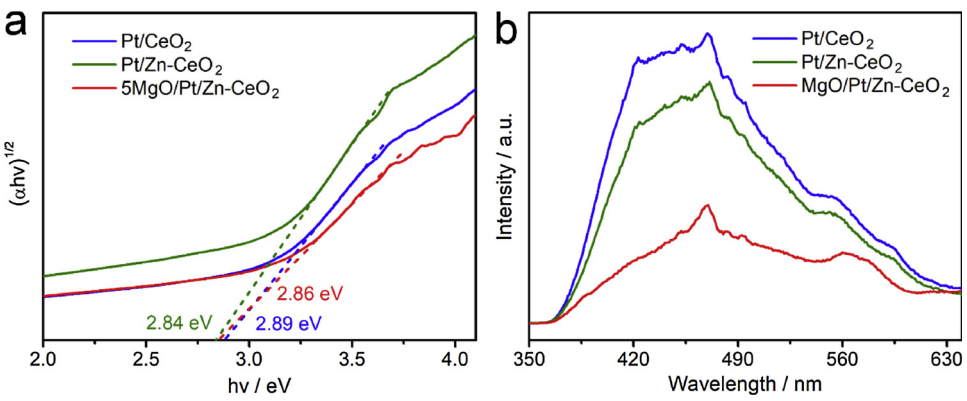

Fig. 2. (a) Band gap measurement using Tauc plot and (b) Photoluminescence spectra for Pt/CeO_2, Pt/Zn-CeO_2, and MgO/Pt/Zn-CeO_2.

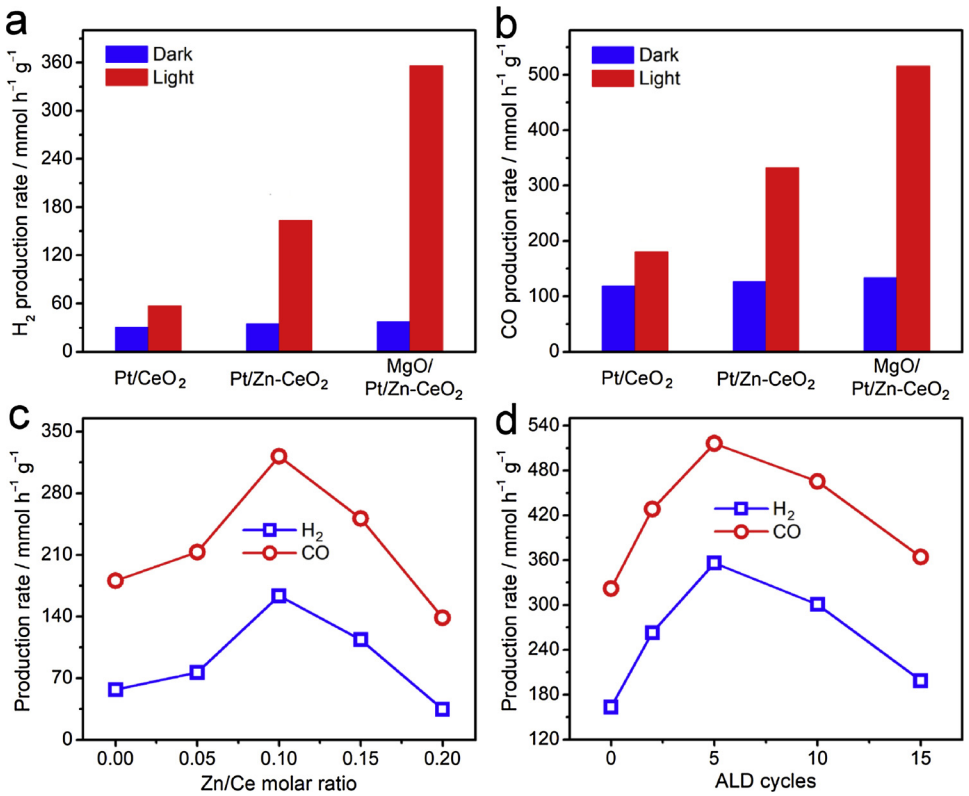

Fig. 3. (a) H_2 and (b) CO production rates at 600 °C in the dark and under light for Pt/CeO_2, Pt/Zn-CeO_2, and MgO/Pt/Zn-CeO_2. (c) The effects of Zn/Ce molar ratio on PTC-DRM activity of Pt/Zn-CeO_2. (d) The effects of ALD cycles on PTC-DRM activity of MgO/Pt/Zn-CeO_2.

and holes and providing abundantly available charge carriers participating in the activation of CO_2 and CH_4, as evidenced by PL tests. The PTC-DRM activities were also collected at different irradiances but at the same temperature (600 °C) (Fig. S8), where the irradiance at 0 sun corresponds to the dark condition at 600 °C. It can be seen that the CO and H_2 production rates show a positive linear tendency with the increasing of irradiance, suggesting a light-dependent characteristic and an increasing photocatalytic contribution to the PTC-DRM process since the temperature was maintained the same. The similar phenomenon has also been observed for PTC-DRM on Pt/TiO_2 at 600 °C [11] and Pt/TaN catalyst at 500 °C [12].

On the other hand, it was found the CO production rates are larger than those of H_2 on all catalysts. In the DRM process, the reaction stoichiometry of CO_2 and CH_4 is 1:1, which ideally gives the same yields for both CO and H_2. Because we did not observe other products, the higher CO yield might be as a result of the occurrence of the reverse water-gas shift reaction (RWGS). In RWGS on Pt-based catalysts, CO_2 reacts with H_2 generating CO and H_2O ($CO_2 + H_2 \rightarrow CO + H_2O$), which has been widely observed and suggested to be a major reason for the lower H_2 yield as compared to CO in the DRM process. [11,32–34] To further confirm this hypothesis, we conducted RWGS on the best-performing MgO/Pt/Zn-CeO_2 by feeding CO_2 and H_2 (3%CO_2/4%H_2/93%Ar) under light irradiation at 600 °C (Fig. S9). The CO generation was confirmed with a rate of about 195 mmol g^{-1} h^{-1}; no other products were observed, which is in a good agreement with previous reports that Pt is very active and selective for CO generation in RWGS. [33,34] This control experiment directly demonstrates that the occurrence of RWGS is responsible for the higher CO yield than H_2.

In the concentrated solar-driven DRM process, there are two possible reactions: thermocatalytic DRM and photocatalytic DRM. The occurrence of thermocatalytic DRM can be evidenced by the production of CO and H_2 in the dark when the reaction temperature is higher than 500 °C (Fig. 4). To demonstrate the photocatalytic effect, we did two control experiments [10]. Firstly, instead of using photoactive CeO_2 semiconductor that can generate photo-excited electrons and holes, we used SiO_2, an insulator, as support to load Pt. As shown in Fig. S10a,b, the H_2 and CO production rates on Pt-SiO_2 under light were almost the same as those obtained in the dark at the same temperature of 600 °C. This demonstrates that the light illumination did not affect the DRM activity on Pt-SiO_2 or cause any photo-thermal effect (i.e. increasing local temperature of Pt due to light illumination). Namely, only the photocatalyst such as CeO_2 as the support is able to enhance DRM activity. Secondly, we conducted the DRM on Pt-free catalysts (Si-doped CeO_2) to further investigate the photocatalytic effects by excluding any possible thermocatalytic effects from Pt. As shown in Fig. S10c,d, the DRM reaction could not occur in the dark; in contrast, both H_2 and CO were produced under light, despite it showed much lower activity compared to Pt-loaded catalysts. This again demonstrates the photocatalytic effects to DRM induced by the photoactive CeO_2 support. The photocatalytic DRM phenomena have also been reported in the literature using different photocatalysts. Hu et al., has demonstrated that photocatalytic DRM can occur on Pt-supported TiO_2 catalyst but not Pt-supported Al_2O_3 above 350 °C [11]. Also, Ye et al., observed photocatalytic DRM on Pt/TaN at 500 °C [12].

We further investigated the effects of Zn contents and ALD cycles on the syngas production rates. As shown in Fig. 3c, Pt/Zn-CeO_2 with a Zn/Ce molar ratio of 0.1 showed the best PTC-DRM activity among other counterparts having various Zn/Ce molar ratios from 0 to 0.2. The H_2 and CO production rates increase gradually as the Zn/Ce ratio increases from 0 to 0.1, which coincides with the trend in the decreased electron-hole recombination, as reflected by PL spectra (Fig. S7a). However, the PTC-DRM activity decreases when the Zn/Ce ratio is larger than 0.15, which is potentially resulted from the declined light absorption (Fig. S6a). As for ALD cycles number that affects the thickness of MgO layers, it was found that the 5 cycles give rise to the highest activity (Fig. 3d). A thin MgO layer may not provide enough contribution to passivate surface states, while a thick MgO coating can prevent the efficient contact between reactants with active CeO_2 surface, as evidenced by

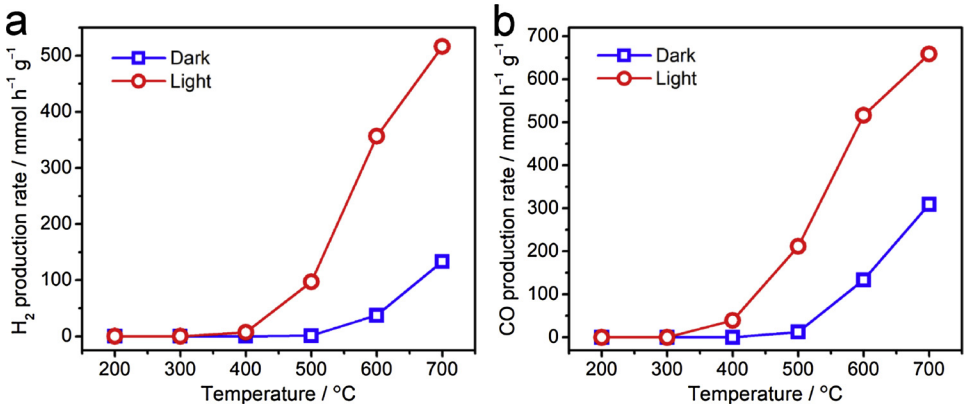

Fig. 4. (a) H_2 yields, (b) CO yields, (c) CO_2 conversions, and (d) CH_4 conversion for DRM on MgO/Pt/Zn-CeO_2 at different temperatures in the dark and under light irradiation.

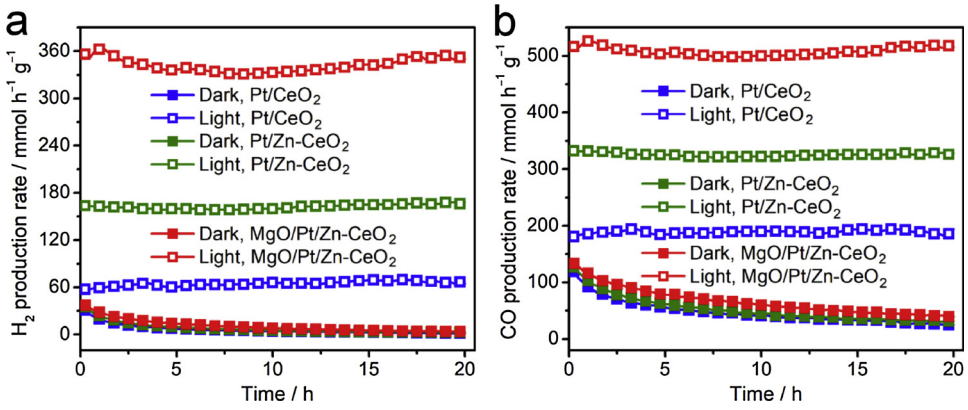

Fig. 5. Long-term DRM stability tests. (a) H_2 and (b) CO production rates for Pt/CeO_2, Pt/Zn-CeO_2, and MgO/Pt/Zn-CeO_2 in the dark and under light irradiation at 600 °C for 20 h.

weaker Ce 2p XPS intensity when more ALD cycles were applied (Fig. S11). Therefore, the balance between optical properties and surface compositions of catalysts governs the overall PTC-DRM activity.

To further understand the photocatalysis contribution in PTC-DRM, we performed DRM at different temperatures both in the dark and under light irradiation conditions. As depicted in Fig. 4, DRM cannot occur at 400 °C or below without light irradiation on MgO/Pt/Zn-CeO_2, which is a typical thermocatalytic characteristic that requires high temperature to activate CO_2 and CH_4 [1]. When the reaction temperature was increased to 500 °C, extremely low yields of 1 and 13 mmol g^{-1} h^{-1} for H_2 and CO were obtained in the dark. By contrast, when the catalyst was irradiated by light, the reaction could occur at a low temperature of 400 °C, which is 100 °C lower relative to that in the dark. At 500 °C under light, the H_2 and CO production rates are 97 and 211 mmol g^{-1} h^{-1}, which are 88 and 17 times higher than those obtained in the dark at the same temperature. Furthermore, H_2 and CO yields increase with increasing of reaction temperatures, indicative of the endothermic nature of thermocatalytic DRM. The higher yields under light as compared to the thermal-driven DRM unambiguously confirm the positive contribution from the photocatalysis process in lowering the reaction temperatures for CO_2 and CH_4 activation and boosting the syngas production rates. The photocatalytic contribution can be further evidenced by higher CO_2 and CH_4 conversions under light irradiation as compared to those obtained in the dark (Fig. S12). Typically, CO_2 and CH_4 conversions were 20.4 and 9.2% in the dark at 600 °C, which increased to 52.6 and 38.8% when MgO/Pt/Zn-CeO_2 was irradiated by light at the same reaction temperature of 600 °C. However, we did not observe the H_2 and CO generated at a temperature below 300 °C, which agrees with the Hu's discovery that photocatalytic DRM can only occur when the reaction temperature is higher than 350 °C on the Pt/TiO_2 catalyst. [11] Both of the literature reports as well as our work reveal an interesting finding that there is a threshold temperature for the photocatalytic effects to have significant contribution, which is against the common wisdom that photocatalytic reaction should occur at room or low temperatures. It is likely because that the initial activation and dissociation of CO_2 and CH_4 are activated mainly by thermocatalytic processes while the photocatalytic processes contribute to the reaction of intermediate products. However, there is no direct evidence at this moment and we will further investigate the mechanism in our future studies.

3.3. Photo-thermo-catalytic DRM stability

In addition to the great enhancement in DRM activity under light illumination, the catalytic stability is also an important concern which describes its capacity for long-term utilization. We further investigated the effects of light irradiation on DRM stability, and the stability in the dark was also measured as references. As shown in Fig. 5, Fig. S13, all three catalysts showed severe deactivation when the reaction was carried out in the dark at 600 °C. By contrast, it is interesting that these catalysts exhibited outstanding PTC-DRM stability without obvious decay when light irradiation was introduced at 600 °C in a 20 h continuous test. This implies that light illumination can improve the durability of thermocatalytic DRM, as also reflected by the stable CO_2 and CH_4 conversions under the light condition but the decreased conversions in the dark (Fig. S14). When further increasing the reaction temperature to 700 °C, it took a long time (2.5 h) to reach stable syngas production (Fig. S15), probably due to severe sintering of CeO_2 and

aggregation of Pt at the beginning of the DRM reaction at 700 °C. This finding is believed to be of great importance for achieving stable syngas production by using the PTC-DRM method because activity deactivation is commonly a big challenge hindering the application of the thermo-driven DRM technique. [32,35]

Generally, there are four main factors that may cause the deactivation in the high-temperature DRM reaction: sintering of CeO_2 support, aggregation of Pt particle, carbon deposition, and consumption of active sites. [32] To figure out why light irradiation can stabilize DRM reaction, the spent catalysts at 600 °C under light irradiation and in the dark were first examined by TEM and XRD. Taking MgO/Pt/Zn-CeO_2 as an example, we found that the spent catalysts showed similar CeO_2 particles sizes (Fig. S16) in the dark and under light illumination. Furthermore, no noticeable Pt aggregation was observed after long-term reaction in both dark and under light (Fig. S16,S17), which are probably because of the enhanced interactions between Pt and CeO_2 support. [1,36,37] In addition, there are no carbon observed after long-term reaction in both dark and under light (Fig. S16,S17). There are two possible reasons to explain the coke-free phenomenon. Firstly, Pt is known as a typical catalyst in DRM having superb ability to resist carbon formation due to the poor catalytic nature towards the C—C bond coupling. [1] Secondly, CeO_2 has been widely demonstrated to be able to remove the deposited carbon via the reaction: $2CeO_2 + C \rightarrow Ce_2O_3 + CO$ CeO_2 [38,39]. Therefore, it is likely that light irradiation did not cause changes in CeO_2 sintering, Pt aggregation, and carbon deposition as compared to the thermal-driven condition.

We thus considered the influences of active sites consumption on long-term DRM stability. In the thermocatalytic DRM process on Pt/CeO_2-based catalyst, Pt is considered as the catalytic site for the breakage of C—H bonds in the CH_4 dissociation. [1,40,41] The CO_2 activation is proposed to occur over the oxygen vacancies of CeO_2 support, [18,37,42] which is believed to be strongly dependent on the contents of oxygen vacancies. Thereby, we performed XPS to analyze the changes in oxygen vacancies concentrations before and after reactions by measuring Ce 3d chemical states for fresh and spent catalysts. To maintain the original states of spent catalysts, we kept the flow of Ar when DRM was terminated until the reaction temperature cooled naturally to the room temperature to prevent the CeO_2 support from being re-oxidized by air at high temperatures, and the spent catalysts were also stored in the Ar atmosphere. As shown in Fig. 6, the Ce 3d XPS spectra can be well split into two species: Ce^{4+} and Ce^{3+}, where Ce^{3+} suggests the formation of oxygen vacancies and a larger Ce^{3+} / (Ce^{3+} + Ce^{4+}) value indicates a higher oxygen vacancies concentration on catalysts surface. [37,43–45] From these spectra, it can be seen that the u2 and v2 peaks, which represent Ce^{4+}, of spent catalysts in the dark have significantly larger percentages than those in pristine and light-spent ones, suggesting that the concentration of Ce^{4+} species increased after the long-term DRM reaction in the dark. Based on the calculated Ce^{3+} / (Ce^{3+} + Ce^{4+}) ratios, it was found that DRM reaction in the dark lead to drastic decreases in Ce^{3+} / (Ce^{3+} + Ce^{4+}) ratios for all these three catalysts. Notably, the Ce^{3+} / (Ce^{3+} + Ce^{4+}) ratios are maintained their initial values when the reaction was conducted under light, implying that the generation of oxygen vacancies took place under light irradiation. Previous studies have shown that the light irradiation could help the effluence of surface oxygen atoms due to the decreased metal-oxygen bond [46,47] and that Ce^{4+} ions can trap photo-excited electrons to form Ce^{3+} and oxygen vacancies. [43] For example, light-induced in situ evolution of oxygen vacancies have been discovered on TiO_2 [47], ZnO [48], CeO_2 [43,45], and BiOCl [46,49]. In our high-energy light irradiation condition, it is inferred that the generation of oxygen vacancies may become easier.

During the thermo-driven DRM, the decrease in oxygen vacancies is resulted from the reoxidation of Ce^{3+} to Ce^{4+} in the CO_2 activation process through $Ce_2O_3 + CO_2 \rightarrow 2CeO_2 + CO$, [32,37] in which an oxygen vacancy will be filled up by the O atom from CO_2 dissociation. It is thus more likely that the consumption of oxygen vacancies results in the observed activity decay in the thermocatalytic DRM due to the suppression of CO_2 dissociation. In contrast, in the photo-thermo-catalytic DRM process, although thermocatalytic CO_2 dissociation can consume oxygen vacancies, they can be regenerated simultaneously under light irradiation, thus retaining the stable activation of CO_2. Therefore, it might be the light-induced recovery of oxygen vacancies on CeO_2 that maintains the stable PTC-DRM activity, as compared to the serious deactivation in the dark condition. In view of these results, the enhanced PTC-DRM activity and stability might stem from the positive contribution from both photocatalysis and thermocatalysis in the solar-thermal process.

3.4. Photo-thermo-catalytic DRM mechanism

As described above, well-designed MgO/Pt/Zn-CeO_2 exhibited excellent photo-thermo-catalytic activity and stability towards CO_2 reforming of CH_4. We here try to discuss the possible catalytic mechanisms. In the thermocatalytic pathway, CH_4 is regarded to be activated on the Pt sites and splitted into C and H (step 1); and the chemical coupling of two H species generates H_2 (step 2). [1,40,41] As for CO_2

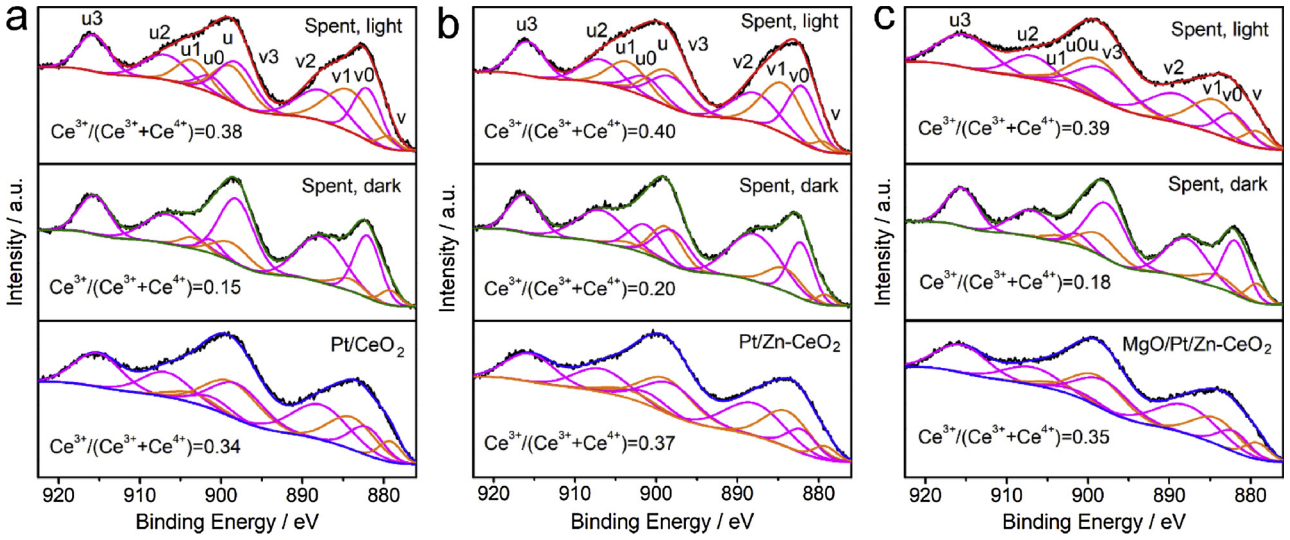

Fig. 6. Ce 3d XPS spectra of pristine and spent catalysts in the dark and under light after 20 h DRM reaction at 600 °C for (a) Pt/CeO_2, (b) Pt/Zn-CeO_2, and (c) MgO/Pt/Zn-CeO_2. u3, u2, u, v3, v2 and v peaks correspond to Ce^{4+}, and u1, u0, v1, and v0 refer to Ce^{3+}.

thermal activation, the dissociation of C − O takes place on the oxygen vacancies (Vo) sites and produce CO and O (step 3), in which the O is mobile and can take part in the removal of step 1-generated C by oxidizing C into CO (step 4). [18,37,42] In the step 3, despite oxygen vacancies are consumed under thermocatalysis, they can be regenerated simultaneously under light irradiation (step 5, step 6), thus stabilizing the thermo-driven DRM process [43,45]. In addition, the reverse water-gas shift reaction (step 7) also occurs accompanying with the DRM process, where CO_2 reacts with H_2 and generate CO and H_2O. [32]

In the photocatalytic DRM process, CeO_2 first adsorb visible and UV light and generate electron (e^-) and hole (h^+) in the bulk of CeO_2 (Step 5), which transport to the surface of CeO_2. CH_4 or intermediates (CH_X) could be oxidized by holes to generate CH_{X-1} and proton (H^+) (step 8). [6] The H^+ can be reduced by electrons to H_2 (step (9)), [50] and the CH_X can be thermocatalytically oxidized by O from step (3) to CO and H_2 (step (10)). [51] On the other hand, it is considered that CO_2 can be photocatalytically reduced to CO_2^- by electron (step (11)), which can be further reduced to CO in the presence of H^+ (step (12)). [52,53] In the overall process, the high-temperature condition facilitates the photocatalytic DRM process, and the light-induced recovery of oxygen vacancies stabilizes the thermocatalytic DRM process. Therefore, the synergy between photocatalysis and thermocatalysis results in the apparent enhanced PTC-DRM activity and stability in the solar thermochemical process as compared to the traditional thermo-driven DRM. However, it has to be pointed out that the exact synergy mechanism may be much more complicated and needs to be further explored in future research.

$$CH_4 \rightarrow CH_3 + H \rightarrow CH_2 + 2H \rightarrow CH + 3H \rightarrow C + 4H \quad (1)$$

$$H + H \rightarrow H_2 \quad (2)$$

$$CO_2 \rightarrow CO + O \quad (3)$$

$$C + O \rightarrow CO \quad (4)$$

$$CeO_2 + hv \rightarrow CeO_2 + e^- + h^+ \quad (5)$$

$$Ce^{4+} + e^- \rightarrow Ce^{3+} + Vo \quad (6)$$

$$CO_2 + H_2 \rightarrow CO + H_2O \quad (7)$$

$$CH_x + h^+ \rightarrow CH_{x-1} + H^+ \quad (8)$$

$$H^+ + H^+ + 2e^- \rightarrow H_2 \quad (9)$$

$$2CH_x + 2O \rightarrow 2CO + xH_2 \quad (10)$$

$$CO_2 + e^- \rightarrow CO_2^- \quad (11)$$

$$CO_2^- + e^- + 2H^+ \rightarrow CO + H_2 \quad (12)$$

4. Conclusions

In summary, we have developed a novel catalyst that comprises atomic MgO layers over Pt supported Zn-doped CeO_2 for photo-thermocatalytic conversion of CO_2 and CH_4 into syngas. The Zn doping and surface MgO modification promote the separation of charge carriers, providing abundant available electrons and holes and thus accelerating CO_2 reduction and CH_4 oxidation. Accordingly, this catalyst showed outstanding PTC-DRM activity with H_2 and CO production rates reaching 356 and 516 mmol $g^{-1} h^{-1}$ under 30 suns irradiations at 600 °C, which are more than 9 and 3 times higher compared to those obtained in the thermally driven DRM at the same temperature. Meanwhile, we demonstrated that light irradiation can keep reforming stability without deactivation in a 20 h test, while the thermocatalytic DRM exhibited the severe deactivation. The mechanistic investigation revealed that light irradiation can induce the in situ generation of oxygen vacancies during the DRM process, which balances the consumption of oxygen vacancies as catalytic sites in the CO_2 thermo-activation process, thus maintaining a durable PTC-DRM process. The findings pave a new way towards the sustainable conversion of greenhouse gases into valuable chemicals via the solar-powered photo-thermo-chemical catalysis process.

Declaration of Competing Interest

The authors declare that they have no known competing financial interests or personal relationships that could have appeared to influence the work reported in this paper.

Acknowledgment

This work was supported by U.S. National Science Foundation (Grant No. 1548091, 1924466, and 1924574).

Appendix A. Supplementary data

Supplementary material related to this article can be found, in the online version, at doi:https://doi.org/10.1016/j.apcatb.2019.118189.

References

[1] D. Pakhare, J. Spivey, Chem. Soc. Rev. 43 (2014) 7813–7837.
[2] K. Mette, S. Kühl, A. Tarasov, M.G. Willinger, J. Köhnert, S. Wrabetz, A. Trunschke, M. Scherzer, F. Girgsdies, H. Düdder, K. Kähler, K.F. Ortega, M. Muhler, R. Schlögl, M. Behrens, T. Lunkenbein, ACS Catal. 6 (2016) 7238–7248.
[3] V. Havran, M.P. Duduković, C.S. Lo, Ind. Eng. Chem. Res. 50 (2011) 7089–7100.
[4] C. Agrafiotis, H. von Storch, M. Roeb, C. Sattler, Renew. Sust. Energy Rev. 29 (2014) 656–682.
[5] B. Tahir, M. Tahir, N.A.S. Amin, Appl. Catal. B Environ. 248 (2019) 167–183.
[6] B. Tahir, M. Tahir, N.A.S. Amin, Appl. Surf. Sci. 419 (2017) 875–885.
[7] B. Tahir, M. Tahir, N.A.S. Amin, Energ. Convers. Manage. 159 (2018) 284–298.
[8] M. Tahir, B. Tahir, Z.Y. Zakaria, A. Muhammad, J. Clean. Prod. 213 (2019) 451–461.
[9] M. Tahir, B. Tahir, N.S. Amin, Mater. Res. Bull. 63 (2015) 13–23.
[10] F. Pan, X. Xiang, W. Deng, H. Zhao, X. Feng, Y. Li, ChemCatChem 10 (2018) 1–7.
[11] B. Han, W. Wei, L. Chang, P. Cheng, Y.H. Hu, ACS Catal. 6 (2016) 494–497.
[12] H. Liu, H. Song, W. Zhou, X. Meng, J. Ye, Angew. Chem. Int. Ed. 57 (2018) 16781–16784.
[13] G. Wang, H. Wang, Y. Ling, Y. Tang, X. Yang, R.C. Fitzmorris, C. Wang, J.Z. Zhang, Y. Li, Nano Lett. 11 (2011) 3026–3033.
[14] R. Asahi, T. Morikawa, T. Ohwaki, K. Aoki, Y. Taga, Science 293 (2001) 269–271.
[15] D. Channei, B. Inceesungvorn, N. Wetchakun, S. Ukritnukun, A. Nattestad, J. Chen, S. Phanichphant, Sci. Rep. 4 (2014) 5757.
[16] M. Sanchez-Dominguez, G. Morales-Mendoza, M.J. Rodriguez-Vargas, C.C. Ibarra-Malo, A.A. Rodriguez-Rodriguez, A.V. Vela-Gonzalez, S.A. Perez-Garcia, R. Gomez, J. Environ. Chem. Eng. 3 (2015) 3037–3047.
[17] X. Xiang, F. Pan, Y. Li, Adv. Compos. Hybrid Mater. 1 (2018) 6–31.
[18] P. Zhang, T. Wang, J. Gong, Chem. Commun. 52 (2016) 8806–8809.
[19] F. Le Formal, N. Tetreault, M. Cornuz, T. Moehl, M. Gratzel, K. Sivula, Chem. Sci. 2 (2011) 737–743.
[20] B. Hoex, J.J.H. Gielis, M.C.M. Sanden, W.M.M. Kessels, J. Appl. Phys. 104 (2008) 113703.
[21] H. Zhao, J. Chen, G. Rao, W. Deng, Y. Li, Appl. Surf. Sci. 404 (2017) 49–56.
[22] X. Feng, F. Pan, H. Zhao, W. Deng, P. Zhang, H.-C. Zhou, Y. Li, Appl. Catal. B: Environ. 238 (2018) 274–283.
[23] M.-G. Jeong, S.Y. Kim, D.H. Kim, S.W. Han, I.H. Kim, M. Lee, Y.K. Hwang, Y.D. Kim, Appl. Catal. A Gen. 515 (2016) 45–50.
[24] X. Li, F. Chen, X. Lu, C. Ni, Z. Chen, J. Rare. Earth. 27 (2009) 943–947.
[25] M.M. Khan, S.A. Ansari, D. Pradhan, D.H. Han, J. Lee, M.H. Cho, Ind. Eng. Chem. Res. 53 (2014) 9754–9763.
[26] P. Quaino, O. Syzgantseva, L. Siffert, F. Tielens, C. Minot, M. Calatayud, Chem. Phys. Lett. 519-520 (2012) 69–72.
[27] S. Tsunekawa, T. Fukuda, A. Kasuya, Surf. Sci. 457 (2000) L437–L440.
[28] N. Wetchakun, S. Chaiwichain, B. Inceesungvorn, K. Pingmuang, S. Phanichphant, A.I. Minett, J. Chen, ACS Appl. Mater. Interfaces 4 (2012) 3718–3723.
[29] L. Li, H.K. Yang, B.K. Moon, Z. Fu, C. Guo, J.H. Jeong, S.S. Yi, K. Jang, H.S. Lee, J. Phy. Chem. C 113 (2009) 610–617.
[30] K. Nagaveni, M.S. Hegde, G. Madras, J. Phy. Chem. B 108 (2004) 20204–20212.
[31] Z. Liu, D.C. Grinter, P.G. Lustemberg, T.-D. Nguyen-Phan, Y. Zhou, S. Luo, I. Waluyo, E.J. Crumlin, D.J. Stacchiola, J. Zhou, J. Carrasco, H.F. Busnengo, M.V. Ganduglia-Pirovano, S.D. Senanayake, J.A. Rodriguez, Angew. Chem. Int. Ed. 55 (2016) 7455–7459.
[32] N. Wang, W. Qian, W. Chu, F. Wei, Catal. Sci. Technol. 6 (2016) 3594–3605.
[33] S. Kattel, P. Liu, J.G. Chen, J. Am. Chem. Soc. 139 (2017) 9739–9754.
[34] M.D. Porosoff, B. Yan, J.G. Chen, Energy Environ. Sci. 9 (2016) 62–73.

[35] R.K. Singha, A. Yadav, A. Agrawal, A. Shukla, S. Adak, T. Sasaki, R. Bal, Appl. Catal. B Environ. 191 (2016) 165–178.
[36] J. Jones, H. Xiong, A.T. DeLaRiva, E.J. Peterson, H. Pham, S.R. Challa, G. Qi, S. Oh, M.H. Wiebenga, X.I. Pereira Hernández, Y. Wang, A.K. Datye, Science 353 (2016) 150–154.
[37] X. Xiang, H. Zhao, J. Yang, J. Zhao, L. Yan, H. Song, L. Chou, Appl. Catal. A Gen. 520 (2016) 140–150.
[38] G.S. Gallego, J.G. Marín, C. Batiot-Dupeyrat, J. Barrault, F. Mondragón, Appl. Catal. A Gen. 369 (2009) 97–103.
[39] S.M. Lima, J.M. Assaf, M.A. Peña, J.L.G. Fierro, Appl. Catal. A Gen. 311 (2006) 94–104.
[40] M. Yang, H. Guo, Y. Li, Q. Dang, J. Nat. Gas Chem. 21 (2012) 76–82.
[41] S. Damyanova, B. Pawelec, K. Arishtirova, M.V.M. Huerta, J.L.G. Fierro, Appl. Catal. B Environ. 89 (2009) 149–159.
[42] T.-J. Huang, H.-J. Lin, T.-C. Yu, Catal. Lett. 105 (2005) 239–247.
[43] T. Ye, W. Huang, L. Zeng, M. Li, J. Shi, Appl. Catal. B: Environ. 210 (2017) 141–148.
[44] G.B. Della Mea, L.P. Matte, A.S. Thill, F.O. Lobato, E.V. Benvenutti, L.T. Arenas, A. Jürgensen, R. Hergenröder, F. Poletto, F. Bernardi, Appl. Surf. Sci. 422 (2017) 1102–1112.
[45] B. Choudhury, P. Chetri, A. Choudhury, RSC Adv. 4 (2014) 4663–4671.
[46] L. Zhang, W. Wang, D. Jiang, E. Gao, S. Sun, Nano Res. 8 (2015) 821–831.
[47] O. Dulub, M. Batzilln, S. Solovev, E. Loginova, A. Alchagirov, T.E. Madey, U. Diebold, Science 317 (2007) 1052–1056.
[48] J. Bao, I. Shalish, Z. Su, R. Gurwitz, F. Capasso, X. Wang, Z. Ren, Nanoscale Research Lett. 6 (2011) 404.
[49] L. Ye, K. Deng, F. Xu, L. Tian, T. Peng, L. Zan, Phys. Chem. Chem. Phys. 14 (2012) 82–85.
[50] L. Yu, Y. Shao, D. Li, Appl. Catal. B Environ. 204 (2017) 216–223.
[51] H. Liu, X. Meng, T.D. Dao, H. Zhang, P. Li, K. Chang, T. Wang, M. Li, T. Nagao, J. Ye, Angew. Chem. Int. Ed. 54 (2015) 11545–11549.
[52] Y.-X. Pan, Z.-Q. Sun, H.-P. Cong, Y.-L. Men, S. Xin, J. Song, S.-H. Yu, Nano Res. 9 (2016) 1689–1700.
[53] M. Li, L. Zhang, M. Wu, Y. Du, X. Fan, M. Wang, L. Zhang, Q. Kong, J. Shi, Nano Energy 19 (2016) 145–155.